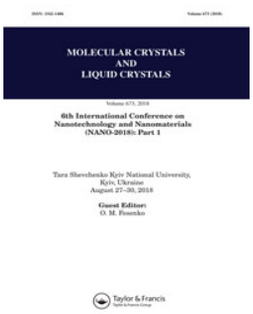

Molecular Crystals and Liquid Crystals

ISSN: 1542-1406 (Print) 1563-5287 (Online) Journal homepage: https://www.tandfonline.com/loi/gmcl20

Structural and electrical properties of nickel-iron spinel/reduced graphene oxide nanocomposites

V. M. Boychuk, V. O. Kotsyubunsky, Kh. V. Bandura, B. I. Rachii, I. P. Yaremiy & S. V. Fedorchenko

To cite this article: V. M. Boychuk, V. O. Kotsyubunsky, Kh. V. Bandura, B. I. Rachii, I. P. Yaremiy & S. V. Fedorchenko (2018) Structural and electrical properties of nickel-iron spinel/reduced graphene oxide nanocomposites, Molecular Crystals and Liquid Crystals, 673:1, 137-148, DOI: 10.1080/15421406.2019.1578503

To link to this article: https://doi.org/10.1080/15421406.2019.1578503

Published online: 19 Jun 2019.

MOLECULAR CRYSTALS AND LIQUID CRYSTALS
2018, VOL. 673, NO. 1, 137–148
https://doi.org/10.1080/15421406.2019.1578503

Taylor & Francis
Taylor & Francis Group

Structural and electrical properties of nickel-iron spinel/reduced graphene oxide nanocomposites

V. M. Boychuk, V. O. Kotsyubunsky, Kh. V. Bandura, B. I. Rachii, I. P. Yaremiy, and S. V. Fedorchenko

Vasyl Stefanyk Precarpathian National University, 57 Shevchenko Str., Ivano - Frankivsk, 76025, Ukraine

ABSTRACT

Nickel iron spinel/reduced graphene oxide composite material was synthesized by simultaneous hydrothermal treatment of nickel and ferric nitrates and graphene oxide colloidal solution obtained using Hummers method. XRD, SEM, Mossbauer spectroscopy, impedance spectroscopy and low temperature nitrogen adsorption were used for materials characterization. The electrical conductivity mechanisms for pure nickel ferrite, reduced graphene oxide and nickel iron spinel/reduced graphene oxide composite were investigated with the determination of activation energy values. Synchronous hydrothermal synthesis of nickel ferrite and the reduction of graphene oxide allow obtaining novel functional material that consists of oxide nanoparticles spaced by carbon fragments.

KEYWORDS

Nckel iron spinel; reduced graphene oxide; hydrothermal synthesis; electrical conductivity; Mossbauer spectroscopy

1. Introduction

Nickel-iron spinels (NIS) with structural formula of $Ni_xFe_{3-x}O_4$ are promising material with the wide range of novel technological applications – spintronic devices [1], as electrode materials for hybrid supercapacitors and Li-batteries [2], catalysis [3], sensors [4], microwave absorbing coating [5], photoelectrochemistry [6], biomedical applications [7] due to a good combination of electronic and magnetic properties. The success of nickel-iron spinels use in many important applications such as supercapacitors and Li-batteries depends on the redox activity and pseudocapacitive behavior under the condition of electrochemical stability that can be achieved by using of ultrafine ferrite particles [8]. The wet chemical methods typically allow synthesis of spinel nanoparticles with the sizes of about 15-25 nm [9, 10], however agglomeration and aggregation processes exclude obtaining of the stable particles with less average diameters. Carbon nanomaterials, in particular, reduced graphene oxide (rGO), are high perspective electrode material for double-layer supercapacitor due to its structural and electrical properties [11]. However, nowadays redox (hybrid) capacitors that operate fast oxidation–reduction reactions that leads to a pseudocapacitive behavior are more attractive. A potential electrode material for high performance hybrid supercapacitors should have the superior redox activity in combination with excellent electron conductivity, high specific surface area and good chemical stability. The composite materials based on the ultrafine oxides

CONTACT V. O. Kotsyubunsky kotsuybynsky@gmail.com

or hydroxides of 3d-transition metals and carbon nanostructures, in particular, rGO are the most promising [12, 13]. In composites highly-dispersed carbon component (rGO fragments) forms conductive bridges between oxide particles enabling high surface redox reactions and pseudocapacitance charge storage mechanism. [14]. Nickel ferrite/rGO systems combine the benefits of both functional materials so the study of the influence of synthesis conditions on the structural, morphological and electrical properties of NIS/rGO composite for obtaining of high performance electrode material is crucial.

2. Experimental details

2.1. Preparation of GO, NIS, and NIS/rGO materials

GO was obtained using Hummers method [15]. The reduction of GO was carrying out under the hydrothermal conditions with the using of hydrazine hydrate.

Ultrafine nickel-iron spinel (NIS) samples were synthesized by hydrothermal method. Nickel nitrate (1.164 g) and ferric nitrate (3.234 g) were dissolved in distilled water (120 ml) under continuous stirring at the room temperature for 25 minutes. The estimated chemical composition of nickel spinel is $(Fe)\ [Fe_{1.6}Ni_{0.4}]O_4$. Sodium hydroxide aqueous solution was added dropwise until pH is 10.0. The obtained sol was sealed into Teflon-lined stainless steel autoclave and heated at 180 °C for 10 hours. The obtained precipitate was separated and washed several times in distilled water until pH is neutral. Finally it was dried at 60 °C for up to mass stabilization to obtain the as-synthesized sample.

At the first stage of NIS/rGO composite material preparation GO sol (80 mg GO dispersed in 60 mL of distilled water via ultrasonication for 120 min) was added to the aqueous solution of nickel nitrate and ferric nitrate with the next slow hydrazine hydrate adding. Then pH value of the obtained colloid was adjusted to 10.0 by adding of 5M NaOH. Last stage of synthesis was performed similarly to carbon-free NIS preparation using hydrothermal route.

2.2. Materials characterization

The phase composition and structure of the synthesized materials were analyzed by XRD and SAXS on a DRON-3M powder diffractometer (Cu Kα radiation). The average size of coherent scattering domains (CSD) was calculated by Scherrer's formula. Morphological properties were investigated by low-temperature nitrogen absorption/desorption (Quantachrome Autosorb Nova 2200e device). Mossbauer spectra were measured with moving absorber using MS1104Em spectrometer with 1.7×10^7 Bq ^{57}Co (Cr) radiation source. Calibration of the isomeric shift was made using α-Fe foil. The velocity resolution was ∼0.006 mm/s per channel. The obtained signal-to-noise ratios were higher than 25. The Mossbauer spectra were measured at the temperature range from 90 to 293 κ in transmission geometry. Chemical composition of the obtained materials was investigated by X-ray fluorescence analysis (Expert 3L device, not less 0.01 mass %)

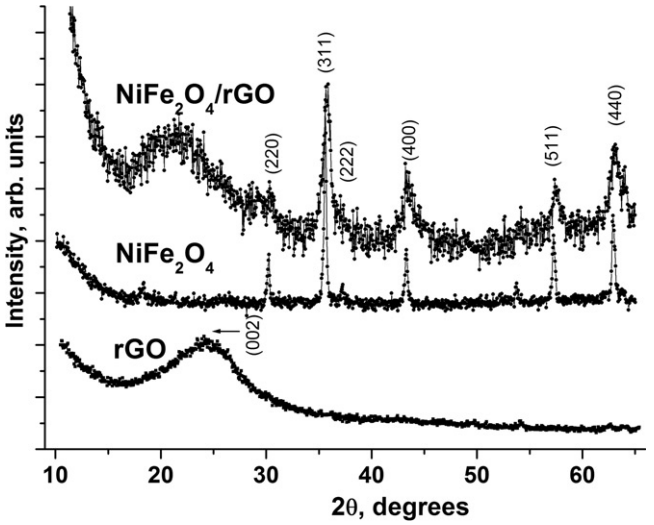

Figure 1. XRD patterns of rGO, NIS and NIS/rGO samples.

3. Results and Discussion

XRD patterns of rGO, NIS and NIS/rGO composite are presented in Figure 1. The XRD pattern for rGO shows broadened characteristic (002) diffraction peak at about 2θ = 25° [16]. The Scherrer's equation $D = \frac{K\lambda}{\beta \cos\theta}$ was used for (002) peak for obtaining information about structural characteristics of the CSD, where K is a shape factor (K = 0.89 for calculation of the average width of stacking layers (L), λ is a wavelength (0.15405 nm), β is a full width at half maximum of peak in radians and 2θ is a peak position on the diffraction pattern [17].

It is determined that the rGO sample consists of coherent scattered packages with average width of about 3.4 nm that equals to 4 - 5 graphene stacked layers. SEM imaging of rGO surface morphology shows the presence of individual plate-like aggregates with an average size of 20-35 nm and width of about 5 nm (Figure 2a).

XRD data for NIS sample corresponds to monophase cubic spinel (cubic, PDF 00-023-1119, a = 0.8367 nm). The average crystallite sizes of nickel-iron spinel phase were about 26 nm. According to SEM images NIS sample consists of prismatic agglomerates with the sizes of about 70-80 nm that are formed by smaller elements with sizes of 15-30 nm (Figure 2b). The peak broadening for NIS/rGO XRD pattern was observed due to decreasing of average particle sizes to about 8-9 nm. The wide halo in 2θ range of 15-27° is a result of rGO component presence. Basal reflection (002) peak for graphite is at 2θ = 26.6° that corresponds to the interplanar distance of 3.35 Å. The shift of characteristic diffraction peak of rGO sample from about 2θ = 24.7° to 2θ = 22.5° corresponds to increasing of average distance between graphene layers from 3.60 to 3.95 Å respectively. The increasing of interplanar distance is an evidence of rGO sheets restacking and rearrangement after reduction carried out simultaneously with the NIS nucleation when the anchoring of spinel nanoparticles on the rGO fragments is possible. NIS/rGO composite material has complex morphology and is formed by merged agglomerates with average particles sizes of about 15-25 nm (Figure 2c).

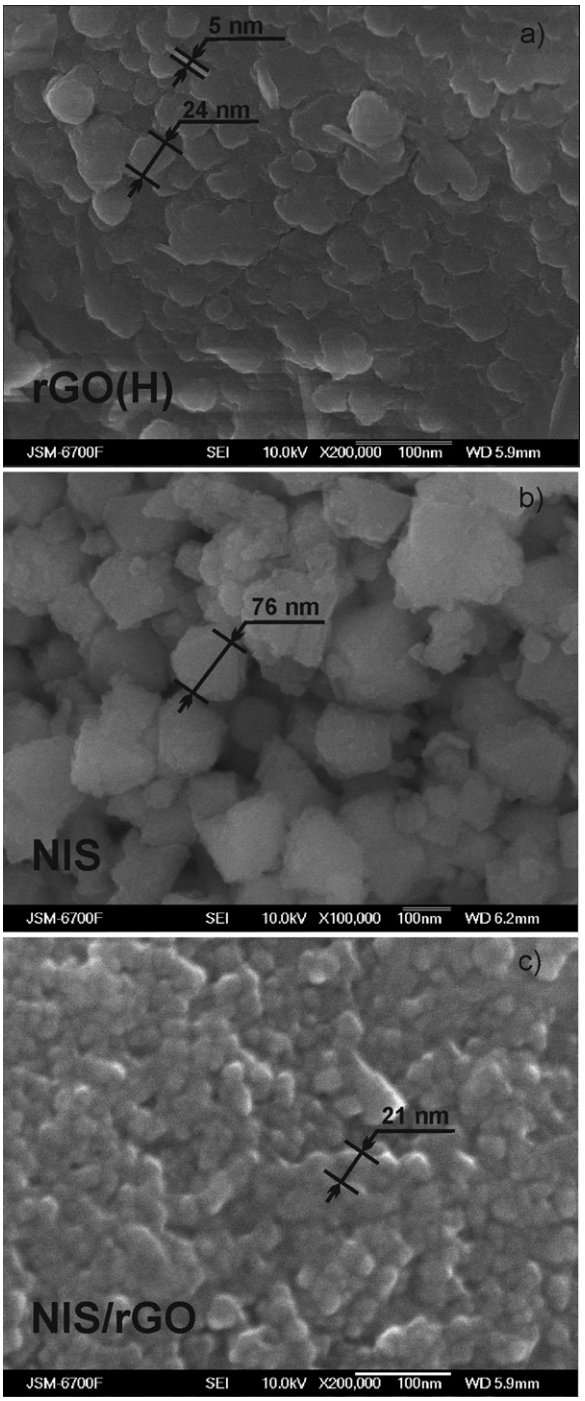

Figure 2. SEM images of (a) rGO, (b) NIS and (c) NIS/rGO samples.

The morphological properties and pore size distribution of the obtained materials were measured using low temperature nitrogen adsorption. As it is shown in Figure 3a the adsorption-desorption isotherm of rGO has IV type with hysteresis type H4 that

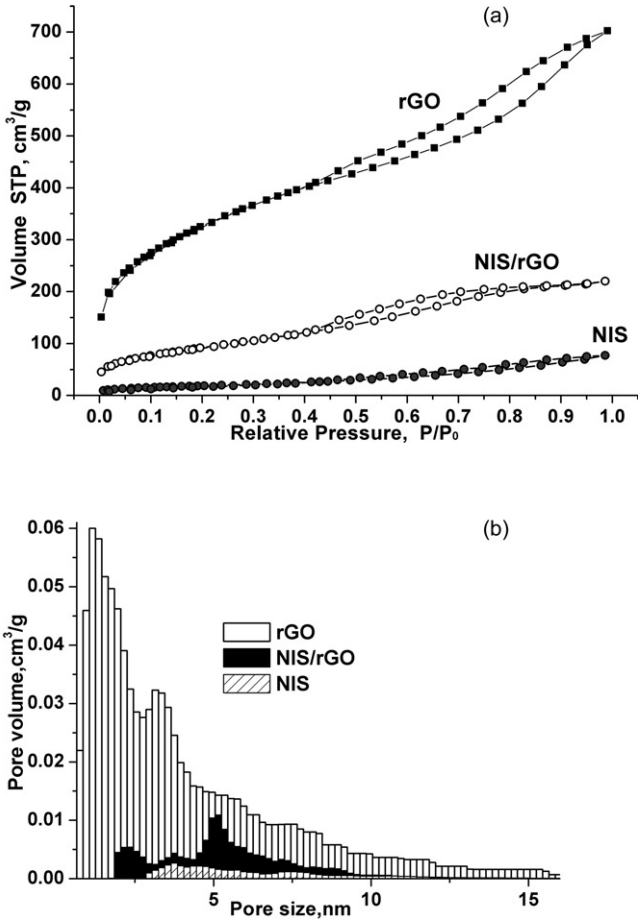

Figure 3. (a) Nitrogen adsorption and desorption isotherms and (b) pore size distributions for rGO, NIS and NIS/rGO samples.

indicates the presence of mesoporosity and is typical for micro-mesoporous carbons [18] This sample has a high value of BET specific surface area (about 1150 m^2/g) and is characterized by wide pore-size distribution with the most probable pore size of about 1.3 nm (Figure 3b). Type IV isotherm was measured also for NIS/rGO composite but H2(b) adsorption hysteresis was observed in this case (Figure 3a) that indicates complex pore structures in which network effects are present with possible pore blocking [18]. This sample has, in general, uniform pore size distribution in a range of 2 - 8 nm with the slight maximum at about 5.1 nm and value of BET specific surface area of about 150-160 m^2/g. Type III isotherm was measured for NIS sample that corresponds to weak adsorbent-adsorbate interactions and accumulation of adsorbed molecules on the favorable surface sites of a low-porous solid. The calculation of pore size distribution for NIS sample with BET area up to 45-55 m^2/g is approximated due to a very weak hysteresis but we can assert the existence of weak mesoporous structure (Figure 3b).

The room temperature Mossbauer spectra of NIS sample consist of a magnetically split sextet with broadened lines typical for ferrimagnetic spinels and a central superparamagnetic part (Figure 4a). The acceptable fit of the experimental spectra was obtained

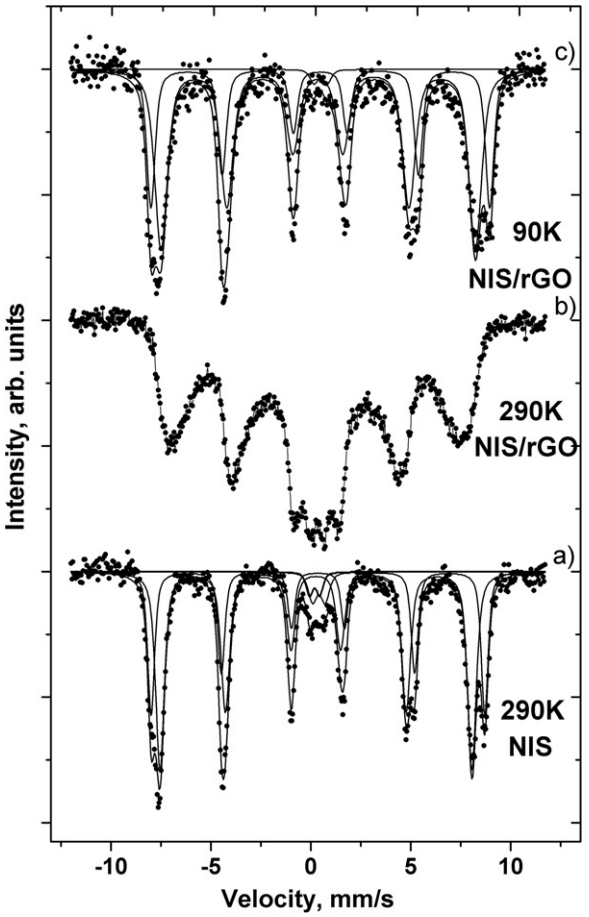

Figure 4. The Mossbauer spectra of NIS/rGO and NIS, samples at room temperature (a), (b) and NIS/rGO at 90 K (c).

using 2 magnetic sextets and 2 superparamagnetic doublets (Table 1). One of the sextets corresponds to Fe^{3+} ions in octahedral sites due to its bigger isomer shift *IS* and bigger hyperfine field *HF* and the second sextet is attributed to Fe^{3+} ions in tetrahedral sites [19].

The value of quadrupole splitting (*QS*) for all magnetic sextet components are close to 0, that corresponds to spherical symmetry of Fe^{3+} ions in the close surrounding that is typical for cubic spinel structure. It is known that the ratio of Fe^{3+} molar contents in tetrahedral (*A*) and octahedral (*B*) sites determines the ratio of relative intensities S_A and S_B of spectra components: $\frac{[Fe_A^{3+}]}{[Fe_B^{3+}]} = \frac{S_A}{S_B} \times \frac{f_B}{f_A}$ [20], where $f_A/f_B = 0.94$ – the ratio of the recoilless fractions for octahedrally and tetrahedrally coordinated Fe^{3+} ions. This allows calculating Fe^{3+} ions distribution between sublattices $(Fe)[Fe_{1.64}Ni_{0.36}]O_4$. The reduction of crystallite size leads to the noncollinear magnetic structure formation due to spin canting in superficial layers of particles [21]. The main reason of this magnetic disordering is rearrangement of low coordinated ions in near-surface regions of particles that leads to disturbing and destruction of *Fe-O-Fe* exchange interaction. As a result the transition of some particles into spin-glass state and further into superparamagnetic

Table 1. Fitting parameters of the Mössbauer spectra of NIS and NIS/rGO samples.

Site	IS, mm/s	QS, mm/s	HF, kOe	S, %	L, mm/s
NIS, T = 295 K					
A	0.36 ± 0.01	−0.003 ± 0.001	518 ± 1	34.1	0.41 ± 0.03
B	0.26 ± 0.01	−0.009 ± 0.002	485 ± 1	59.2	0.52 ± 0.03
D_1	0.19 ± 0.01	0.51 ± 0.02	–	2.5	0.40 ± 0.04
D_2	0.41 ± 0.02	0.62 ± 0.02	–	4.2	0.52 ± 0.05
NIS / rGO, T = 90 K					
A	0.48 ± 0.02	0.001 ± 0.001	526 ± 2	35.4	0.50 ± 0.04
B	0.36 ± 0.02	0.017 ± 0.002	488 ± 3	63.1	0.76 ± 0.05
D	0.49 ± 0.03	0.66 ± 0.03	–	1.5	0.48 ± 0.04

IS– Isomeric Shift; QS – Quadrupole Splitting; HF– Hyperfine Field; S - Relative Integral Intensity; L - Line Width.

state is possible. It can be assumed that two paramagnetic doublet components correspond to Fe^{3+} ions in the inner and outer regions of ultrafine spinel particles. The probability of superparamagnetic transition depends on the relaxation time τ_r of particle magnetic moment fluctuation: $\tau_r = \tau_0 \exp\left(\frac{KV}{kT}\right)$, where $\tau_0 \asymp 10^{-9}$-10^{-11} s, V– particle volume, K– constant of magnetic anisotropy, T– temperature. The superparamagnetic effects are observed when τ_r become less than τ_{lf} =141.8 ns (lifetime of ^{57}Fe nucleus excited state). The constant of magnetic anisotropy of NIS is about (5-6)· 10^5 J/m^3 [22]. The estimated threshold size of nickel iron spinel particles with fluctuated magnetic moments at room temperature is about 9 nm. The Mossbauer spectra of NIS/rGO material at room temperature consist of broadened sextets and doublets due to the presence of ultrafine ferrite particles with superparamagnetic behavior (Figure 4b). It is clear that the simultaneous synthesis of ferrite and reduced graphene oxide has a direct effect on the size of the spinel particles and causes its decreasing. Additional information about magnetic microstructure of this sample was obtained using low temperature Mossbauer spectroscopy (Figure 4c, Table 1). The main difference between NIS/rGO Mossbauer spectra at 90 K and pure NIS at room temperature is the increasing of line width L for all components and increasing of quadrupole splitting for octahedrally coordinated ^{57}Fe nuclei. The average content of doublet component for these spectra do not exceed 1.5% that corresponds to the presence of ferrite particles fraction with the size of about 3-4 nm. Calculated cation distribution for NIS/rGO can be written as $(Fe)[Fe_{1.68}Ni_{0.32}]O_4$.

The frequency dependencies of specific electric conductivity σ measured at different temperatures allow investigating the influence of materials microstructure and morphology on the charge carriers transferring. The systematic growth of rGO electric conductivity with the temperature increasing was observed. The decreasing of electrical conductivity of the rGO at frequencies bigger than 1000 Hz is explained by skin effect (Figure 5a). Charge carriers at high frequencies form electric current only in the near-surface region of particles. The electric field strength drops exponentially with the distance from the particles surface. $\sigma(T)$ curves in this case can be described by Drude model of electron collisions and are fitted using equation: $\sigma(T) = \frac{\sigma_{dc}}{1+\omega^2\tau^2(T)}$, where σ_{dc} is a direct current conductivity and τ is the most probable collision time. The monotonous growth of both σ_{dc} and τ with temperature increasing was observed for rGO sample. The thermally activated carrier movement at low frequency follows Arrhenius law with the temperature increasing: $\sigma_{dc} = \sigma_0 \exp\left[-\frac{E_a}{kT}\right]$, where σ_0 is a temperature independent constant, T is an absolute temperature and k is Boltzmann constant [23]. Activation

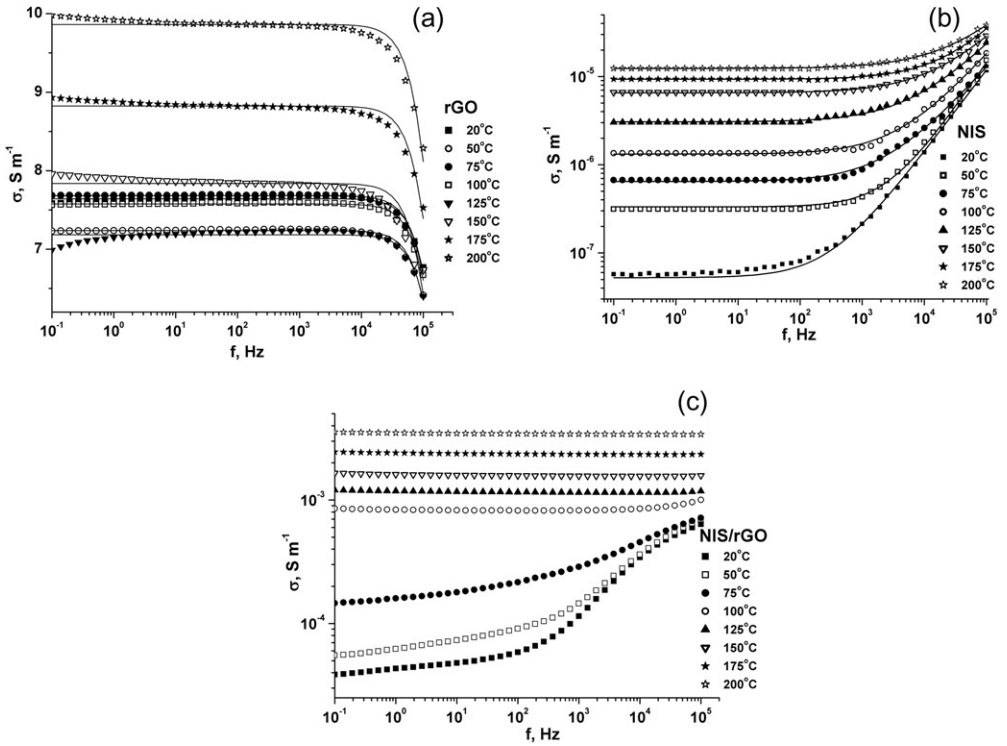

Figure 5. AC conductivity with varying frequency at different temperatures of the (a) rGO, (b) NIS and (c) NIS/rGO samples.

energy E_a values obtained by fitting of Arrhenius plots $ln(\sigma_{dc})(1/T)$ are of about 0.07 ± 0.01 eV (Figure 6b).

The plot of $\sigma(f)$ for NIS sample consists of two regions – frequency-independent region at low-frequencies and frequency- sensitive one (Figure 5b). In the case of frequency-independent *dc* conductivity the charge carriers transfer is carried out through the thermal activated random diffusion traps when frequency dependency of electrical conductivity corresponds to its correlated motion. The $\sigma(\omega)$ dependencies for NIS sample for the temperature range of 20-200 °C were fitted by Johnsher model [24] that predict electron percolation in the crystal potential under the electric field under the condition of polarization effects: $\sigma_{AC}(\omega) = \sigma_{dc} + A\omega^n$, where σ_{dc} is a frequency independent conductivity, A is a dispersion parameter and n is a dimensionless frequency exponent that is the measure of the degree of interaction $0<n<1$ (n = 0 and for an ideal Debye dielectric dipolar-type and n = 1 for an ideal ionic-type crystal). The temperature dependence of $\sigma_{dc,}$ A and n are presented in Figure 7a and Figure 7b respectively

Typical for spinel ferrites percolation conductivity mechanism is based on the polaron theory and is described by thermally activated electrons hopping between localized states of multivalent transition metals cations located on octahedral sites of the spinel structure [25]. The activation energy values of this process depend on the cation type, path of the superexchange interaction, crystal stoichiometry, concentration of defects and morphological features of the material. It is known that activation energy of

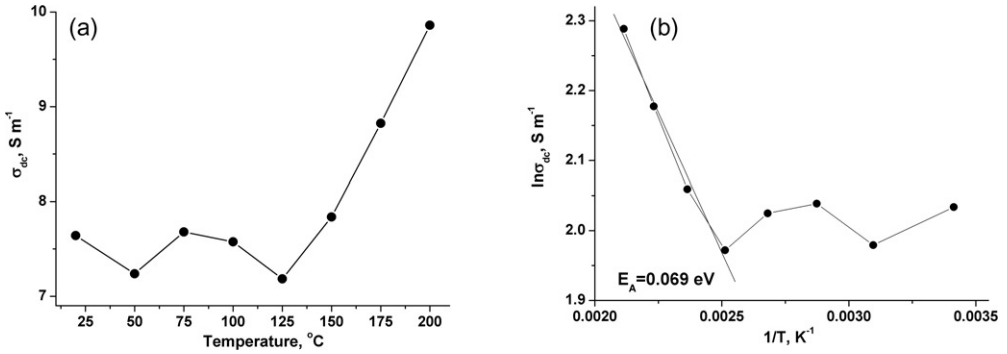

Figure 6. (a) The temperature dependences of electrical conductivity and (b) the Arrhenius dependencies of ln(σ) vs T^{-1} for rGO sample.

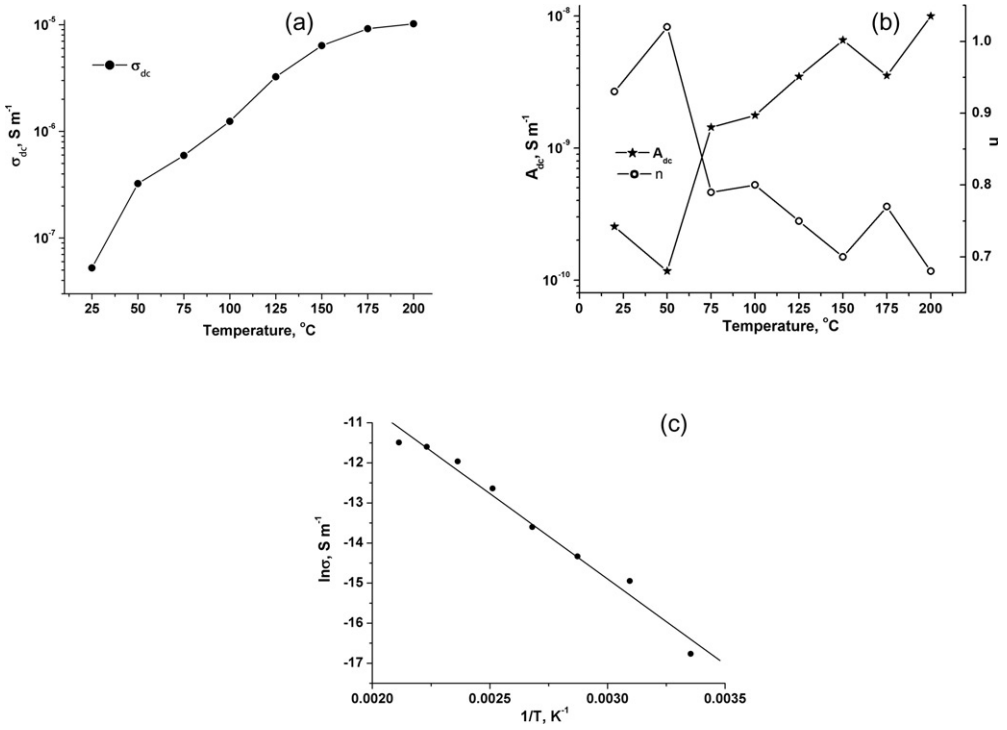

Figure 7. Variations of (a) σ_{dc} and (b) characteristic parameters (A and n) of Johnsher's fits with temperature for NIS sample and (c) Arrhenius plot for this material.

electrical conductivity for spinel systems, in particular for NIS varies for bulk grain and grain boundary and it is a function of the grain size [26]. The activation energy value that is calculated from slope between $ln(\sigma_{dc})$ and $1/T$ depends on the temperature (Figure 7c). The obtained value (E_a = 0.37 ± 0.02 eV) is close to reported ones. For example, electrical conductivity of bulk NIS is caused by electron hopping between Fe^{2+} and Fe^{3+} ions and hole hopping between Ni^{3+} and Ni^{2+} ions and has the value of an average activation energy of about 0.45 eV [27]. The temperature dependence of frequency exponent is determined by the changes of interaction degree between mobile

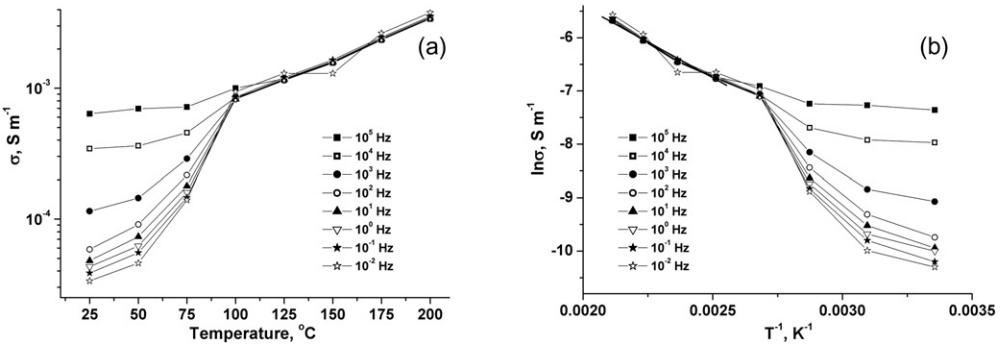

Figure 8. (a) σ vs. T and (b) ln(σ) vs. T^{-1} plots with fitted linear regions of the NIS/rGO sample for different frequencies.

ions and the lattice around them. The decreasing of n values with temperature increasing corresponds to domination of large polaron hopping mechanism [28]. The observed behavior of n at 25 and 50 °C can be explained by effects of localization and delocalization of hopping charge carriers when e_g electrons energy is less than electrostatic energy applied by grain boundaries. The formation of conductive channels happens for hopping of localized d-electrons through superexchange paths Fe^{3+} - O - Fe^{2+} and Ni^{2+} - O - Ni^{3+}. The decreasing of power law exponent (n) range corresponds to overlapping large polaron tunneling mechanism of conductivity when correlated barrier hopping mechanism is most probable for higher than 75 - 100 °C.

The complex temperature dispersion of the electric conductivity NIS/rGO composite material at different frequencies was observed (Figure 5c). Figure 8a shows the temperature dependence of *dc* conductivity of the sample at some representative frequency. The σ values at six selected frequencies were used for determination of activation energy (E_a) for polaron mechanism. Very close dependencies were observed for all used frequencies in temperature range 100-200 °C The Arrhenius plots of $ln(\sigma)$ vs T^{-1} were linearized for this temperature range (Figure 8b). The calculated value of activation energy electric conductivity for NIS/rGO composite material is E_a = 0.23 ± 0.01 eV.

The temperature changes of composite sample's conductivity can be explained using next model. NIS/rGO material can be described as an array of oxide particles spaced by partially conjugated carbon fragments. The charge carriers motion for rGO component is associated with π-electrons hopping traps along $-C = C-$ bonds between basal planes of separate graphene layers in the rGO packages. The presence of high conductive carbon component is crucial for efficiency of d-electrons hops between the separate NIS particles. In this case transferring paths of the charge carriers are formed by both superexchange chains like Me^{3+} - O - Me^{2+} and motion through conductive band of graphene fragments [29]. It is clear that the efficiency of percolation process must be frequency sensitive. The frequency increase leads to the increasing of percolation probability at temperatures below the threshold value (100°C) (Figure 6a). The electrical properties of the NIS/rGO became frequency independent in the temperature range of 125-200 °C that can indicate the fact that

electron hopping in graphene component became the dominant type of electrical conductivity (Figure 5c).

4. Conclusion

In summary, nickel-iron spinel/reduCed graphene oxide (NIS/rGO) composite materials was synthesized by a hydrothermal route. The investigations of structural, morphological and electrical properties of NIS/rGO and its component (NIS and rGO samples) were performed. It was observed that the simultaneous synthesis of NIS and GO reduction leads to forming of composite system as an array of oxide particles with average sizes of about 15-25 nm spaced by partially conjugated carbon fragments. A presence of rGO component with good electrical conductivity forms a percolation path for conduction in the low conduction spinel ceramic. The processing of frequency-dependent conductivity spectra allows the separate different types of charge transferring. It was determine that the percolation-type though hopping of d-electrons between 3d-metals ions with different oxidation degree dominates for NIS/rGO up to about 100 °C with increasing of influence with frequencies growth. Temperature dependencies of electrical conductivity for composite material at the temperature range of 100-200 °C became frequency independent with domination of the π-electrons hopping conductivity with energy activation value of 0.24 ± 0.02 eV.

References

[1] Moodera J. S., Miao G. X., & Santos T. S. (2010). *Phys. Today*, 63(4), 46.
[2] Javed M. S., Zhang C., Chen L., Xi Y., & Hu C. (2016). *J. Mater. Chem. A*, 4(22), 8851.
[3] Morales M. R., Barbero B. P., & Cadús L. E. (2007). *Appl. Catal., B*, 74(1-2), 1.
[4] Reddy C.V., Gopal S. V. Manorama, & V. J. Rao. (1999). *Sens. Actuators, B*, 55(1), 90.
[5] Gu X., Zhu W., Jia C., Zhao R., Schmidt W., & Wang Y. (2011). *Chem. Commun.*, 47(18), 5337.
[6] Zhang X., Xu H., Li X., Li,Y., Yang T., & Liang Y. (2015). *ACS Catal.*, 6(2), 580.
[7] Silva M. N., Duque J. G. D. S., Gouveia D. X., de Paiva J. A., & Macedo M. A. (2004). *Jpn. J.Appl. Phys.*, 43(8R), 5249.
[8] Gunjakar J. L., More A. M., Gurav K. V., & Lokhande C. D. (2008). *Appl. Surf. Sci.*, 254(18), 5844.
[9] Chen D. H., & He X. R. (2001). *Mater. Res. Bull.,* 36(7–8), 1369.
[10] George M., John A. M., Nair S. S., Joy P. A., & Anantharaman M. R. (2006). *J. Magn. Magn. Mater.*, 302(1), 190.
[11] Zhao B., Liu P., Jiang Y., Pan D., Tao H., Song J., & Xu W. (2012). *J. Power Sources*, 198, 423.
[12] Tang Z., Tang C. H., & Gong H. (2012). *Adv. Funct. Mater.*, 22(6), 1272.
[13] Xiang C., Li, M., Zhi M., Manivannan A., & Wu N. (2013). *J. Power Sources*, 226, 65.
[14] Wang H. W., Hu Z. A., Chang Y. Q., Chen Y. L., Wu H. Y., Zhang Z. Y., & Yang Y. Y. (2011). *J. Mater. Chem.*, 21(28), 10504.
[15] Alam S. N., Sharma N., & Kumar L. (2017). *Graphene*, 6(01), 1.
[16] Compton O. C., & Nguyen S. T. (2010). *small*, 6(6), 711.
[17] Stobinski L., Lesiak B., Malolepszy A., Mazurkiewicz M., Mierzwa B., Zemek J., & Bieloshapka I. (2014). *J. Electron Spectrosc. Relat. Phenom.*, 195, 145–154.
[18] Thommes M., Kanek, K., Neimark A. V., Olivier J. P., Rodriguez-Reinoso F., Rouquerol J., & Sing K. S. (2015). *Pure Appl. Chem.,* 87(9-10), 1051.
[19] Yehia M., Labib S., & Ismail S. M. (2014). *Phys. B*, 446, 49.

[20] Jacob J., & Khadar M. A. (2010). *J. Appl. Phys.*, 107(11), 114310.
[21] Kotsyubynsky V., Moklyak V., & Hrubiak A. (2014). *Mater. Sci.-Pol.*, 32(3), 481.
[22] Karpova T. S., Vasil'ev V. G., Vladimirova E. V., & Nosov A. P. (2012). *Inorg. Mater.: Appl. Res.*, 3(2), 107.
[23] Chakraborty K., Chakrabarty S., Pal T., & Ghosh S. (2017). *New J. Chem.*, 41(11), 4662.
[24] Jonscher A. K. (1996). *Universal Relaxation Law: a Sequel to Dielectric Relaxation in Solids*, Chelsea Dielectrics Press: London, UK.
[25] Hosseinpour A., Sadeghi H., & Morisako A. (2007). *J. Magn. Magn. Mater.*, 316(2), e283.
[26] Ponpandian N., Balaya P., & Narayanasamy A. (2002). *J. Phys.: Condens. Matter*, 14(12), 3221.
[27] Abdeen A. M. (1999). *J. Magn. Magn. Mater.*, 192(1), 121.
[28] Mandal S. K., Singh S., Dey P., Roy J. N., Mandal P. R., & Nath T. K. (2017). *Philos. Mag.*, 97(19), 1628.
[29] Moni P., Wilhelm M., & Rezwan K. (2017). *RSC Adv.*, 7(60), 37559.